Hindawi
Structural Control and Health Monitoring
Volume 2023, Article ID 9972511, 14 pages
https://doi.org/10.1155/2023/9972511

Research Article

High-Order Fiber Bragg Grating Corrosion Sensor Based on the Detection of a Local Surface Expansion

Vedran Budinski, Matej Njegovec, Simon Pevec, Boris Macuh, and Denis Donlagic

University of Maribor, The Faculty of Electrical Engineering and Computer Science, 46 Koroska Cesta, Maribor 2000, Slovenia

Correspondence should be addressed to Vedran Budinski; vedran.budinski@um.si

Received 3 January 2023; Revised 9 July 2023; Accepted 13 July 2023; Published 26 July 2023

Academic Editor: Sara Casciati

This paper presents a fiber optic sensor for the detection of corrosion processes that occur on metal surfaces. In the proposed sensor design, a sensing fiber with an inscribed high-order Bragg grating is attached to the observed metal surface. A broadening of high-order Bragg grating spectral characteristics is observed and used to detect small and highly localized longitudinal strain variations that occur along the fiber as a result of corrosive rust flakes' formations beneath the sensing fiber. The proposed approach provides a straightforward fabrication method, the possibility for unobtrusive mounting, including mounting of the sensor beneath the corrosion-protective layers, and consistent corrosion detection yields.

1. Introduction

Health monitoring of structures in the civil, aerospace, and maritime industries is important to guarantee the maximum lifespan of these structures and ensure the safety of their users. One of the most important processes to monitor in different structures which incorporate metals or metal alloys is corrosion. Statistics indicate both a direct and indirect economic impact of corrosion. Global costs associated with the appearance of corrosion processes in the industry, agriculture, transportation, and service sectors are estimated to be about 3.4% of GDP [1]. Therefore, adequate corrosion prevention measures must be employed to mitigate unwanted material degradation and financial losses. Typical procedures against corrosion include, for example, protective coatings, primers, and special surface treatments. Even if the necessary prevention measures are implemented, deterioration of the structure is possible, and if not detected on time, can cause major corrosion-related failures, even involving personal injuries, fatalities, unscheduled shutdowns, and environmental pollution. Therefore, corrosion sensor systems are vital for efficient online monitoring of a variety of metal or metal containing structures. Currently, there are various reported sensor systems for direct or indirect corrosion detection based on different sensing principles [2], including electrochemical [3–6], ultrasonic, magnetic flux leakage [7], inductive [8], galvanic [9–11], and also employing a nonconductive special sensing textile [12]. Electrical and electrochemical-based corrosion sensing solutions can exhibit shortcomings, for example, being difficult to implement in remote locations, highly corrosive environments, electromagnetically polluted environments, or environments exposed to geoelectric events. Fiber optic sensors (FOSs), on the other hand, have the potential to provide effective corrosion detection solutions. An all-dielectric design, small size, light weight, flexibility, insensitivity to electromagnetic interference, and intrinsic resistance to chemically aggressive environments makes FOS especially suitable for demanding corrosion sensing applications. There are several FOS solutions for corrosion detection which utilize different sensing approaches [13–16]. One principle of operation employs fiber Bragg grating (FBG) corrosion sensors based on tensile stress relaxation and volume expansion [17–23]. In the first case, i.e., tensile stress relaxation detection, the fiber is pretensioned; thus, when the corrosion occurs, the relaxation of the fiber grating instigates a wavelength shift. In the second case, i.e., sample volume expansion, the fiber with the inscribed grating is

fixed, for example, on a surface of round steel sensing rod, whose diameter increases due to the corrosion, and therefore, instigating a tensile strain of the grating, and consequently, shifting the wavelength. This type of sensor provides simple fabrication; however, they lack in the ability to perform long term corrosion monitoring. The other principals exploit coating the fiber with special sensing films. Authors have reported sensors where special Fe-C or Ni-P sensing films were deposited on the fiber with inscribed FBGs or onto fibers with removed cladding [24–30]. In the first case, interaction with the alloy film initiates the relaxation of the pretensioned FBG, thus shifting the optical spectrum of the grating. In the second case, the sensing film is applied to the region without the cladding, thus changing the output optical signal when the film is exposed to the corrosive environment. The above-described sensors are however appropriate only for detecting the early stages of corrosion. Another feasible approach employing FBGs for structural health monitoring in composite structures presents measurements of nonuniform strain [31–43]. In these cases, the host material was bent or elongated with an unequally distributed outer force, thus instigating strain perturbations with the same magnitude. These strain perturbations were then transferred to the fiber's core. Sensor response in the presence of the nonuniform strain exhibited not only spectral shift but also spectral broadening and reflectivity decrease. The levels of the resulting broadening were also modeled and assessed [32–35]. Other in situ corrosion monitoring fiber optic sensors use a fiber loop interferometer based on a photonic crystal fiber (PCF) [44, 45], where the pressure/force change instigated by corrosion modulates the birefringence. Another interesting corrosion discovery solution is presented in [46], where a measuring cell employing an unclad sapphire fiber waveguide operating in the visible spectral range is capable of detecting iron ions released due to the formation of rust. Authors have reported a corrosion sensor based on a tapered polymer optical fiber [47], where the accumulated corrosion between the steel and the sensor produces strain, which translates into the change of optical power transmission of the sensor. Fabry–Perot-based corrosion sensors [48] were also reported in the past for corrosion sensing. However, they require relatively complex mounting setups. The application and mounting of FOS for corrosion detection present a special challenge. In many instances, unobtrusive mounting or possibly sensor mounting beneath the corrosion protective layers is desired, which is limited mostly by the existing FOS sensing principles. The advantage of fiber optic sensors for corrosion detection is also in the possibility to operate in distributed and quasidistributed configurations [49–52].

In this paper, we propose a fiber optic sensor for direct corrosion sensing based on the detection of random local surface volume expansions, which are caused by the corrosion process. This detection is achieved by the implementation of high-order Bragg gratings, which act as surface nonuniformity/roughness detectors. The proposed sensor features a simple design, fabrication technique, and interrogation method. Also, the sensor provides the means of early-stage corrosion detection with simple attachment onto the observed structure. Due to the operation principle and interrogation method, the sensor can easily be configured in a quasidistributed configuration.

2. Principle of Operation, Sensor Design, and Sensor Fabrication

2.1. Principle of Operation. The appearance of corrosion on the surface of a metal is accompanied by local and random volumetric surface expansions, which increase the roughness of the observed surface. Volumetric surface expansion is usually manifested as a random growth of rust flakes and oxide layers on the surface of the corroding material, with dimensions ranging typically from a few to a few tens of micrometers. The detection of these random surface perturbations can be exploited to identify and signal the process of the corrosion progressions. The latter can be accomplished by properly designed fiber Bragg gratings (FBGs), to measure the nonuniform strain along the fiber instigated by the corrosion process.

When a fiber Bragg grating (FBG) is fixed to a flat, uncorroded surface, the inscribed FBG's dielectric mirrors are distributed evenly and fully periodically along the fiber, which results in a narrow back-reflected optical spectrum (Figure 1(a)). If the surface beneath the FBG is perturbed locally and randomly by the appearance of corrosion products, which appear in the form of rust flakes, distances between the inscribed FBG's dielectric mirrors also become distributed unevenly, due to the creation of localized and random longitudinal strain variations along the fiber. The latter causes Bragg grating spectrum degradation, which is reflected in the FBG's spectral peak broadening and peak amplitude reduction (Figure 1(b)). The magnitude of the spectrum degradation depends on the intensity and spatial distribution of the local perturbations and the system for attachment of the sensing fiber to the observed surface. Evaluation and detection of an FBG peak spectral broadening can, thus, be utilized for sensing the onset of a corrosion process.

2.2. FBG Selection. Typical lengths of ordinary/commercial FBGs for strain and temperature sensing applications usually range from 5 to 20 mm [53–55]. In corrosion sensing, however, larger FBG lengths are desired to obtain sensor response over larger physical areas that are more representative of the structural health state. FBGs with lengths ranging from a few centimeters to a few tens of centimeters (or more) would thus be desired [56–58]. The experimental FBGs in this investigation were inscribed with a femtosecond laser employing the point-to-point technique (P-t-P). During the investigation, we performed several attempts using different FBG inscription recipes/procedures, and the spectral line width of the inscribed FBGs always dispersed when we attempted to inscribe long-length 1^{st}-order FBGs. Therefore, in the proposed experimental designs, we utilized femtosecond laser-inscribed FBGs of the 50^{th} to 100^{th} orders, with distances between the mirrors between 25 and 55 μm,

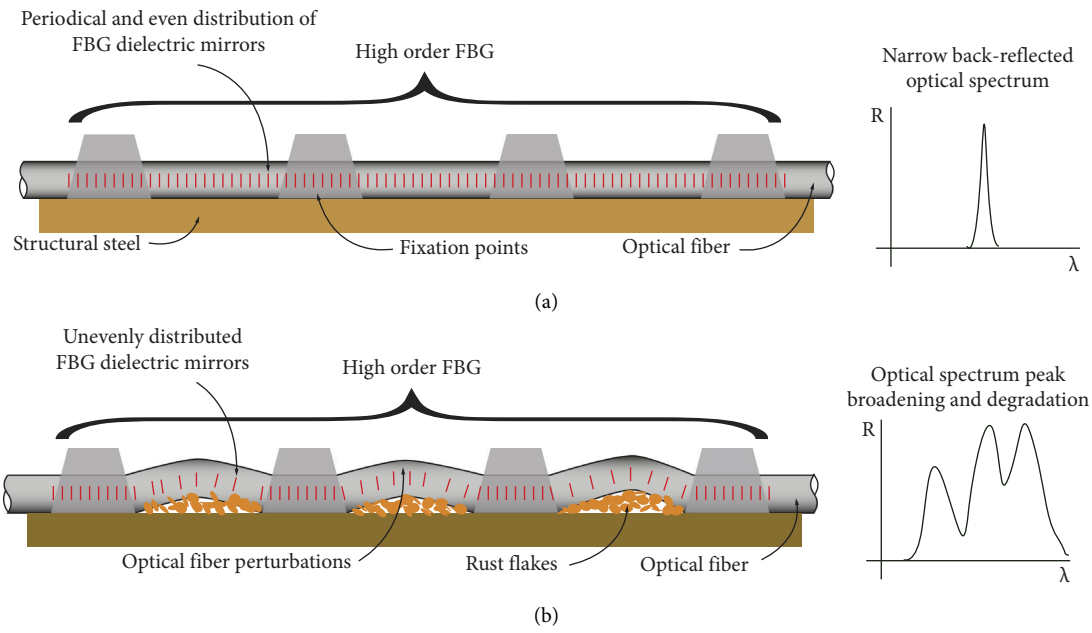

Figure 1: Principle of operation (a) when no corrosion is present and the inscribed dielectric mirrors are distributed periodically along the fiber, thus generating a narrow back-reflected optical spectrum and (b) when corrosion is present, perturbations of the optical fiber instigate distance variations of the inscribed dielectric mirrors and, therefore, the degradation of the optical spectrum.

respectively. These high-order gratings with substantially spaced mirrors provided narrow initial spectra, even when fabricated over substantial lengths of fiber. The FBGs were inscribed in polyimide-coated single-mode fibers (acquired from Fibercore) with cladding diameters of 125 μm, 80 μm, and 50 μm and with polyimide coating thicknesses of 30.3 μm, 22.8 μm, and 21.6 μm, respectively. The typical length of each grating was about 40 mm (and was limited by the linear motors used in our FBG inscription system). FBG fabrication recipes were developed to achieve a typical 2% peak reflectance, and the initial spectral line width between 100 pm and 180 pm for the prepared gratings. It should be stressed that the initially narrow FBG spectral line width is preferred since it defines the sensitivity of the proposed approach (small deviations in FBG bandwidth can be identified more clearly in gratings with an initially narrow spectrum).

2.3. Simulation. To obtain better insight into the proposed principle of operation, we performed a series of finite element (FEM) simulations to determine the degree of strain variation within the fiber core caused by rust product formation beneath the fiber. This included the application of a simplified model, which assumed periodic attachment of the fiber to the observed metal surface (using filler material as the adhesive), while allowing for formation of rust products beneath the unattached fiber. The latter were modeled as the fiber's vertical displacements caused by force/pressure created beneath the fiber. Strain ε_t within the center of the fiber in a direction which is tangential to the path of the fiber's core (Figure 2(a)) was calculated as a function of structure length as follows:

$$\varepsilon_t = \sqrt{\varepsilon_x^2 + \varepsilon_y^2}, \quad (1)$$

where ε_x and ε_y represent the strain components in the vertical and horizontal structure's dimensions. The force in the simulation beneath the fiber was always distributed over an area that had a length of 300 μm and a width corresponding to the length of a 100° ark, as indicated in Figure 2(b). The applied force/pressure was perpendicular to the structure's longitudinal axis. The abovementioned model is presented in Figure 2(c). Fixture points, i.e., the assumed use of a filler material with a width of 1 mm and a height of 0.5 mm with side angles of 25°, this geometry, and the use of filler mimicked a real situation in one of the experiments described in detail in Section 2.3. Furthermore, the modeled fibers, with different diameters, were fixed between two filler fixtures. The length of the modeled fiber was 4 mm, where 1 millimeter from each modeled fiber side was fixed in the modeled fixtures (defined as a bonded contact region in the FEM simulation software), thus leaving 2 mm of the fiber for exposure to external influences. The modeled filler fixtures were fixed in the model at their bottom side. The mesh size for both filler fixtures was set to 50 μm and for the fiber model to 10 μm. The material properties (Young's modulus) of the filler and the optical fiber in the simulation were set to 3000 MPa and 74800 MPa, respectively.

In the performed simulations, 2 mm distances between fiber fixture points were selected, while the widths of the fixtures were 1 mm each, thus mimicking one segment of the actual filler stencil used later in the experimental verification. All the simulations were performed for fibers with outer diameters of 50 μm, 80 μm, and 125 μm.

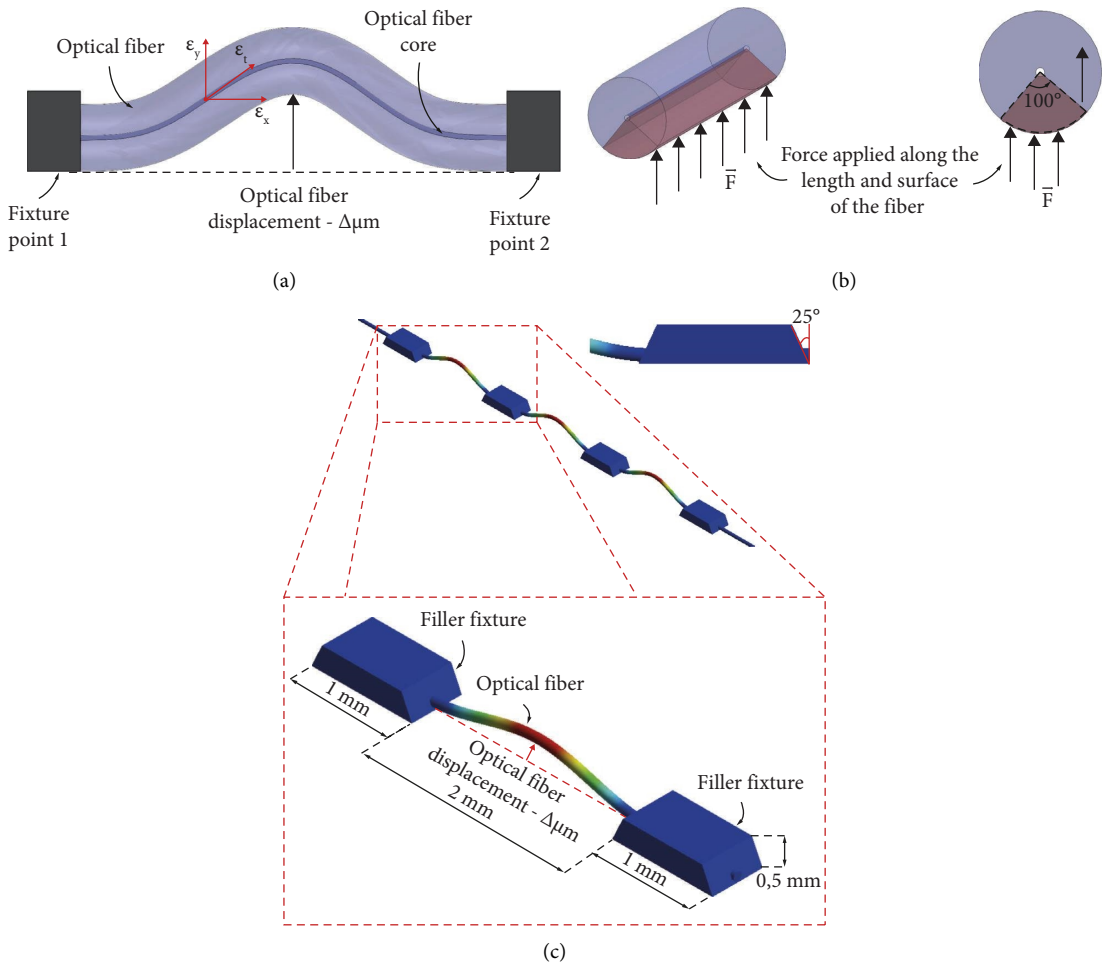

FIGURE 2: (a) Strain distribution within the center of the fiber (core) in a direction which is tangential to the path of the fiber's core ε_t. The optical fiber is fixed between two fixture points (fixture point 1 and fixture point 2) and displaced by a predefined height $\Delta\mu$m. (b) The surface beneath the optical fiber, where the force was applied. (c) The proposed model of the sensor setup of three segments.

In the first set of simulations, the vertically applied force beneath all three types of fiber was varied/increased until the vertical displacement had not reached the predetermined vertical displacements of 50 μm, 75 μm, and 100 μm, which mimicked the formation of rust flakes with a constant size. The results are shown in Figures 3(a)–3(c) for all three fibers. These simulations assumed that the flake rust formation creates fiber displacements with constant magnitude, and that the rust flake formation beneath the fiber was not affected by the presence of the fiber, which inevitably creates back pressure/forces onto the rust flake during its formation. The amplitudes of strain variation along the fiber core, indicated by the red arrows in Figure 3, are within the range of about 50–100 $\mu\varepsilon$ for a vertical displacement of 75 μm (a typical grain height measured experimentally), which predicts splitting of the original FBG peak by about 50–100 pm at 1550 nm (e.g., the FBG spectral strain sensitivity corresponds to about 1.1 pm/$\mu\varepsilon$). The results in Figure 3 also suggest that strain variation amplitude increases with increasing fiber diameter, which would indicate a more sensitive sensor when applying larger diameter sensing fibers. The above performed set of simulations, which assumed constant vertical fiber displacement and ignored the fiber's mechanical feedback on the rust flake growth, might, however, be oversimplistic. During the rust flake formation, the fiber is vertically displaced progressively, which generates force to the growing rust flake (an area underneath the fiber), which might suppress the flake's growth. It is thus important to stress that the set of performed simulations apply to a simple situation with a displacement induced at a single point underneath a double-clamped optical fiber section. This results in the creation of nonuniform strain along the FBG, which further causes spreading of initially narrow FBG optical spectrum as described in Section 2.1. This evolution of strain caused by vertical displacement of in two-point clamped circular beam represents a reasonable approximation of the conditions encountered in the proposed sensor. Furthermore, longitudinal strain evolution in two-point clamped cross-section beams was also well researched, modeled and verified by numerous simulations in the past [59–64]. Simulations carried out within this investigation showed dependency of the geometry of the clamps, i.e., different shapes (angles and height) and clamping materials can significantly affect the longitudinal

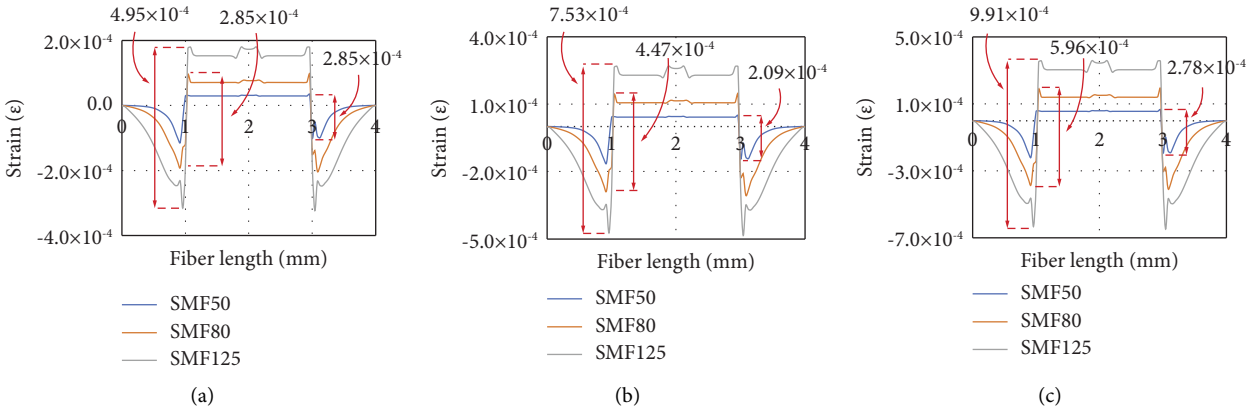

Figure 3: Simulation results, presenting the strain distribution within the center of the fiber's core in a direction which is tangential to the path of the fiber's core when fibers with the diameters of 50 μm, 80 μm, and 125 μm were displaced by (a) 50 μm, (b) 75 μm, and (c) 100 μm.

strain distributions. Also, modeling of a corrosion product is a complex conundrum. There are reported contributions on modeling and simulations of corrosion processes [65–68] and the effects of deposition of corrosion products [69]; however, they focus on temporal distributions of chemical species, potential, and current, to predict corrosion locations and regions, and to elaborate the influence on the microstructure of the material. To best of our knowledge, in the current literature, the effect of the generated corrosion product on displacement has not yet been investigated in the way this paper does. It is, however, meaningful to examine the evolution of the strain along the fiber core when fibers with different diameters are used in the proposed structure, while asserting the same deformation forces to the sensing fiber. Therefore, the simulations presented in Figure 3 were repeated, however, by assuming that the formation of a rust flake induces constant force onto the fiber rather than constant displacement. While the reality is likely in-between both cases, it is expected for one of these two "ideal" cases to prevail. From the simulation assessment, it can be expected that the rust flake formation, which will instigate sensing fiber displacements from 70 μm to 130 μm beneath and around the sensor, will initiate spectrum degradation (broadening) with a magnitude corresponding to a few tens of picometers. Also, due to the sporadic generation of rust flakes along the length beneath the sensor, an uneven spread of the FBG spectral peak is probable.

Figure 4(a) shows the strain distribution along the fiber core while applying the force of 36 mN to the fibers with diameters of 50 μm, 80 μm, and 125 μm. The results indicate a substantially nonlinear relationship between the fiber diameter and the induced strain variation along the fiber. Fibers with smaller diameters yielded significantly higher strain variations when exposed to the same vertical force, so for example, when displacing the fiber with a constant force, the reduction of fiber diameter from 125 μm to 80 μm increases the strain variation along the fiber by a factor of about 3.15, while, when displacing both fibers with the same vertical displacement amplitudes, the same reduction in fiber diameter yielded a decrease in longitudinal strain variation by a factor of 1.69. Furthermore, the simulation results indicate that when the same force was applied, the fiber with the smallest diameter (in the simulation the one with the diameter of 50 μm) exhibited the largest displacement, while the fiber with the largest diameter (125 μm) showed the smallest change in the displacement (Figure 4(b)). To investigate/demonstrate the dependence of the strain amplitude variation versus fiber diameter under constant force and constant displacement conditions further, an extended set of simulations was performed, as shown in Figure 5. In this set of simulations, fibers with different diameters were first displaced by 75 μm, while calculating the amplitude of the strain variation induced by this displacement. Then, the calculated strain variations were normalized by a strain variation which was obtained in the case of the thickest (160 μm diameter) fiber. These data are displayed by the orange curve in Figure 5 and indicate that an increase in the fiber`s diameter increases the amplitude of the strain variation nearly linearly along the fiber's core, when the fiber is displaced by a constant displacement. Then, the force needed to cause displacement was re-applied to the same set of fibers with different diameters, while recalculating (and normalizing) the variation of the strain along the fiber's core. These results are shown by the blue curve in Figure 5 and indicate a significantly nonlinear increase in the amplitude of the strain variation when reducing the fiber's diameter. This pronounced nonlinear relationship between the fiber diameter and the strain variation obtained under constant force conditions indicates that the diameter of the fiber might be a decisive factor which determines the sensor's sensitivity to rust flakes formation, i.e., a substantial reduction in the fiber's diameter shall yield higher-sensitivity sensor structures.

2.4. Realization of the Test Sensors. The inscribed 100th-order FBGs were mounted on the observed surfaces/samples by two approaches:

2.4.1. Attachment of the FBGs with an Adhesive Stencil and Spray Filler. Mounting the sensor on the test sample surface was realized in several steps by employing masking tape and

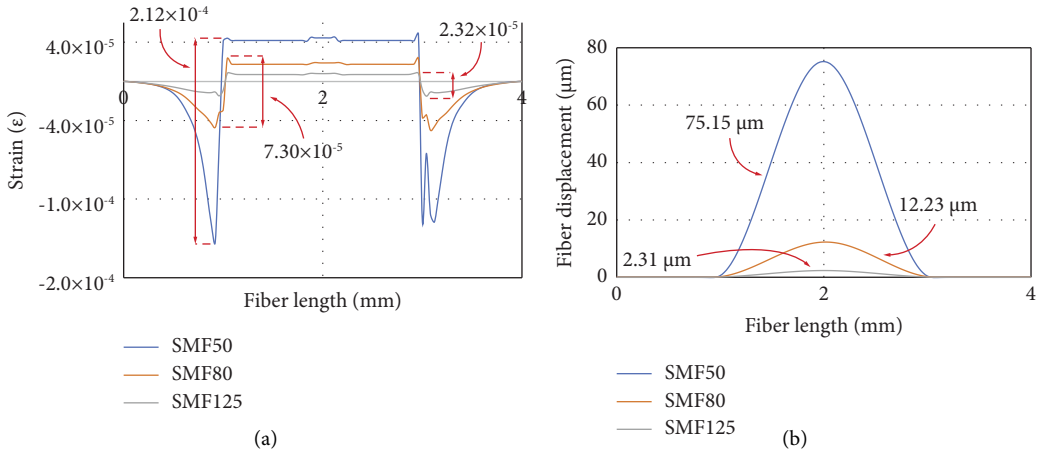

Figure 4: (a) Simulation results, presenting the strain distribution within the center of the fiber's core in a direction which is tangential to the path of the fiber's core when on fibers with diameters of 50 μm, 80 μm, and 125 μm was applied the same force, which on the fiber with the diameter of 50 μm instigated the displacement 125 μm. (b) Displacement of fibers with diameters of 50 μm, 80 μm, and 125 μm, when the same force was applied.

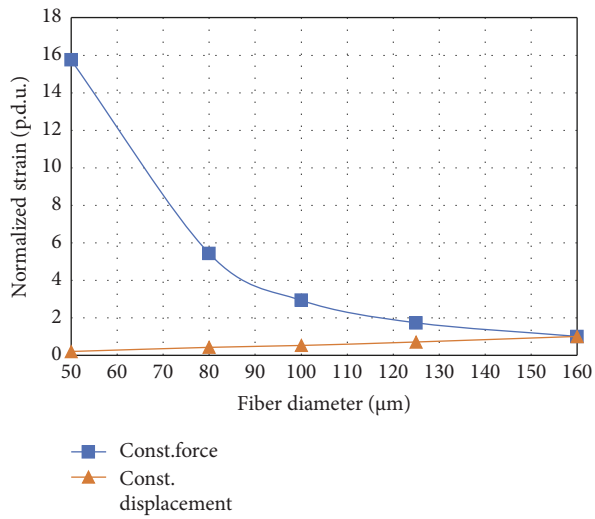

Figure 5: Simulation results presenting the calculated normalized longitudinal strain difference when employing constant force (36 mN) and constant displacement (75 μm) on fibers with diameters 50 μm, 80 μm, 100 μm, 125 μm, and 160 μm.

a spray filler (primer). The masking tape was utilized for devising an adhesive stencil with periodical cut outs. The fiber (sensor) was positioned on the sample and fixed with the cut mask tape. The spray filler was applied afterwards over the stencil in three layers. After the filler was partly cured, the stencil was removed, thus leaving the left-over filler to cure fully for 24 hours. Optionally, a corrosion-protective layer was applied to the above-described setup.

2.4.2. Mounting the FBGs Only with the Protective Paint Coat. This procedure employed mounting the sensor on the test sample surface only with a protective coating, without the adhesive stencil and spray filler. The sensor was pre-tensioned and fixed on the steel sample with high adhesion tape at two points, i.e., at 5 mm before the beginning and 5 mm after the end of the inscribed grating. The sample was coated with 3 thin layers of a protective primer. After the first coat was partly dried, the adhesion tapes were removed, followed by applying the remaining two layers of the primer on the sample.

An algorithm for periodical recording and storing of the FBG's spectral characteristics was prepared within the LabVIEW development environment, which was also used to process the acquired data.

3. Experimental Setup

The proposed corrosion sensing system is presented in Figure 6. The sensor setup consists of a lead-in 125 μm fiber, a sensing polyimide-coated optical fiber with inscribed high-order Bragg grating mounted on the metal sample as described in the previous section, a spectral interrogator (National Instruments PXIe-4844), and a personal computer with the LabVIEW development environment. All the sensors were mounted on a bright structural steel S235JR + C (according to EN) sample.

The tests were conducted by using two different corrosion accelerating approaches. The first approach employed an atmosphere with added hydrochloric acid (HCl) and water vapors. The other approach utilized a saltwater bath with a 5% concentration of NaCl dissolved in demineralized water. The first test procedure was nonstandard but quicker and simpler, thus allowing a large number of tests, which were necessary to identify proper sensor design. The second test procedure was however designed and performed according to American Society for Testing and Materials (ASTM) standard no. G31-21, which empowered sensor operation/response under standardized test conditions. A provisional test chamber (tank) was prepared for both principles. In tests with the acidic atmosphere as the corrosion accelerator, the chamber was equipped with a fan, thus ensuring the circulation of the acid vapors. When the

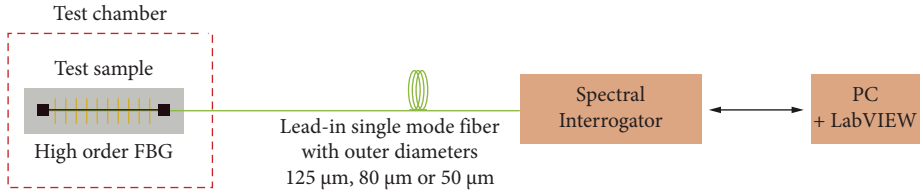

FIGURE 6: High-order FBG corrosion sensor system setup consisting of a spectral interrogation system, a PC with a LabVIEW development system, a lead-in 125 μm, 80 μm, or 50 μm single mode optical fiber with inscribed high-order Bragg grating mounted on a steel sample.

tests were conducted in a saltwater bath to accelerate the corrosion process, an additional heater with a regulating system was installed, to stabilize the water at a temperature of 35°C [70]. The chamber was also equipped with a rotary pump and a bubbler to ensure continuous liquids' oxygenation. With all the tests, the spectral data from the sensor were recorded every 24 hours.

The effect of the corrosion process induces grating spectrum degradation and broadening; thus, the acquired back-reflected spectral characteristic was processed with a suitable algorithm to extract a parameter that reflected the spectral broadening. This algorithm included regression of the Gaussian function over a spectral peak, while calculating the weighted spectral dispersion parameter (σ) of the regressed Gaussian function, which was used further as a corrosion indication parameter. The amount of spectrum distribution was, thus, evaluated by calculating the weighted dispersion parameter (σ) according to

$$\sigma = \sqrt{\frac{\sum_{i=1}^{N} y_i (x_i - x_0)^2}{((N-1)/N)\sum_{i=1}^{N} y_i}}, \quad (2)$$

where x_i is the discrete wavelength in the acquired spectrum and x_0 is the central (weighted) wavelength of the observed peak, calculated as $\sum(x_i \cdot y_i)/\sum y_i$. N is the number of samples and y_i is the spectral density at wavelength x_i. For better intuitive presentation of the spectrum dispersion around the calculated mean wavelength, the result was presented as normalized spectral dispersions (σ/σ_0), where σ_0 is the initial dispersion parameter at the beginning of the test, i.e., right before exposing the sample to the corrosion environment, at $t = 0$.

4. Experimental Results

The first set of tests was conducted using 100$^{\text{th}}$-order FBG sensors based on polyimide-coated fibers with an outer diameter of 125 μm, mounted on an uncoated steel sample surface with the method an employing adhesive stencil and spray filler described in the above text. The sensors were placed in the chamber, equipped with a fan for vapor circulation, and exposed to the hydrochloric acid (HCl) and demineralized water vapors for roughly 16 days. The first unambiguous appearance of spectrum broadening occurred after about 40 h during accelerated testing. Within this phase there were evident visual signs of a formed corrosion on the sample, i.e., the appearance of a rust layer in the areas between the filler strips. The initial spectral widths of the used FBGs corresponded to 0.160 nm and 0.165 nm. The spectrum readouts from the sensors indicated corrosion-induced spectral broadening in the range between 0.7 nm and 0.72 nm (Figure 7(a)). The result tallied to a normalized spectral dispersion σ/σ_0 increase from 1 to up to 4.5, as shown in Figure 7(b).

The second set of tests was conducted by employing sensors based on a single-mode fiber with an outer diameter of 80 μm, and with inscribed 100$^{\text{th}}$-order FBGs in the length of 40 mm. As in the previous test, the sensors were mounted on the steel sample surface with an adhesive stencil and spray filler. The test samples were also exposed to the same corrosion-accelerating atmosphere, comprised of HCl and demineralized water, as described in the previous test case. The duration of a typical test was in the range between 14 and 18 days. After the test, the Bragg grating spectrum readouts indicated significant spectral broadening and spectral peak magnitude decrease, when compared to the tests utilizing fibers (sensors) with a 125 μm outer diameter (Figure 8(a)). Initially, 0.11 nm, 0.12 nm, and 0.14 nm wide sensors' spectrums broadened to 2.1 nm, 1.7 nm, and 1.8 nm, respectively, corresponding to a normalized spectral dispersion σ/σ_0 increase from 1 to up to 19 (Figure 8(b)).

To inspect the sample visually throughout the test, a camera was mounted on the lid of the chamber. The images were recorded at the same time interval as the spectral data from the sensor (every 24 hours). Figure 8 presents the images and spectrums recorded at the beginning, middle and end of the test. A noticeable incidence of a rust flake layer was evident in the areas between the filler stripes (Figure 9(b)). The spectrum broadening increased with additional accumulation of the rust particle layers instigated by the acidic atmosphere in the test chamber (Figure 9(c)).

A reference test on a nonmetal sample was also conducted, to evaluate and exclude the potential adverse cross-effect of the corrosive atmosphere on the spray filler, which might cause undesired effects on the high-order grating spectral characteristics. In this test, the sensing fiber was mounted on the microscope glass slide by the same method as on a metallic sample, employing an adhesive stencil and spray filler (Figure 10(c)). The sample was exposed to the acidic atmosphere in the same way as the metal samples in the tests described in the above text. The results indicated a spectrum shift, which can be attributed to the temperature oscillations in the laboratory (Figure 10(a)) during the test. After exposing the sample to the acidic atmosphere for 18 days, there was no noticeable decrease in the spectrum amplitude or significant spectral broadening (Figure 10(b)).

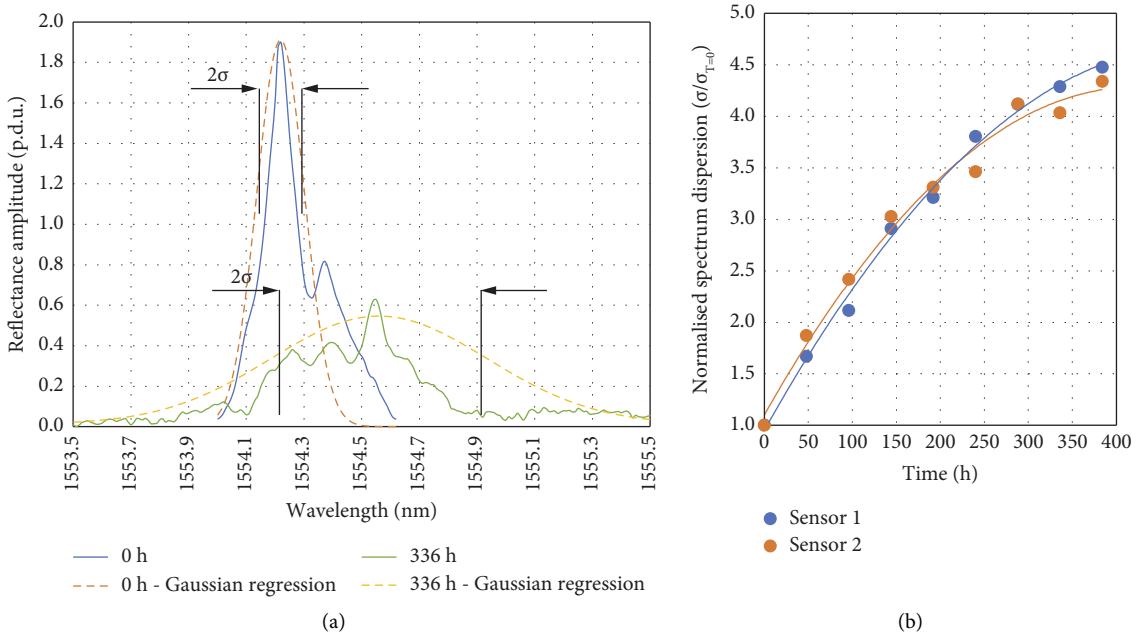

FIGURE 7: (a) Recorded spectrum from the 125 μm sensor fixed with spray filler on a steel sample at the beginning and at the end of the test with the Gaussian regression for the respective measurement. (b) Calculated normalized spectrum dispersion (σ/σ_0) at different time intervals during the test.

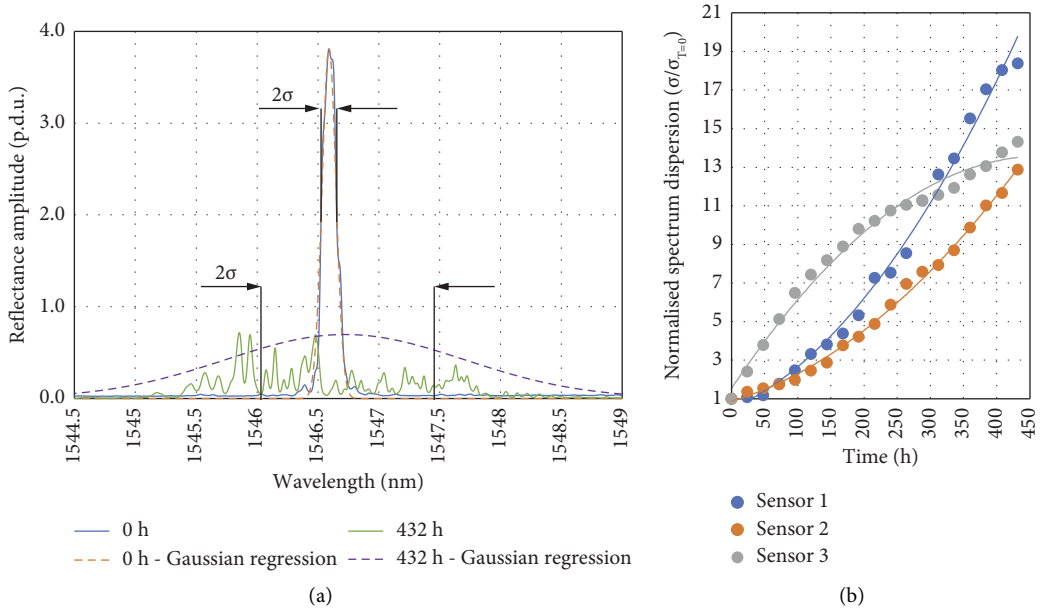

FIGURE 8: (a) A typical recorded spectrum from the sensor fixed with spray filler on a steel sample at the beginning and at the end of the test with the Gaussian regression for the respective measurement. (b) Calculated normalized spectrum dispersion at different time intervals during the test. Normalized with initial dispersion σ at the beginning of the test ($t = 0$).

Minor measured oscillations in the normalized spectral dispersion probably arose from the polarization sensitivity of the used FBGs, long-term filler curing/drying, and the overall long-term stability of the setup. Although a dedicated temperature test was not systematically designed and conducted within this investigation, the tested sensors were exposed to different temperatures during testing and temperature did not significantly affect the spectral broadening. Temperature variations instigated only the spectral shift of the entire FBG characteristics in the wavelength domain without affecting their width during the corrosion tests.

The high sensitivity achieved by the 80 μm diameter fiber encouraged further testing by further application of

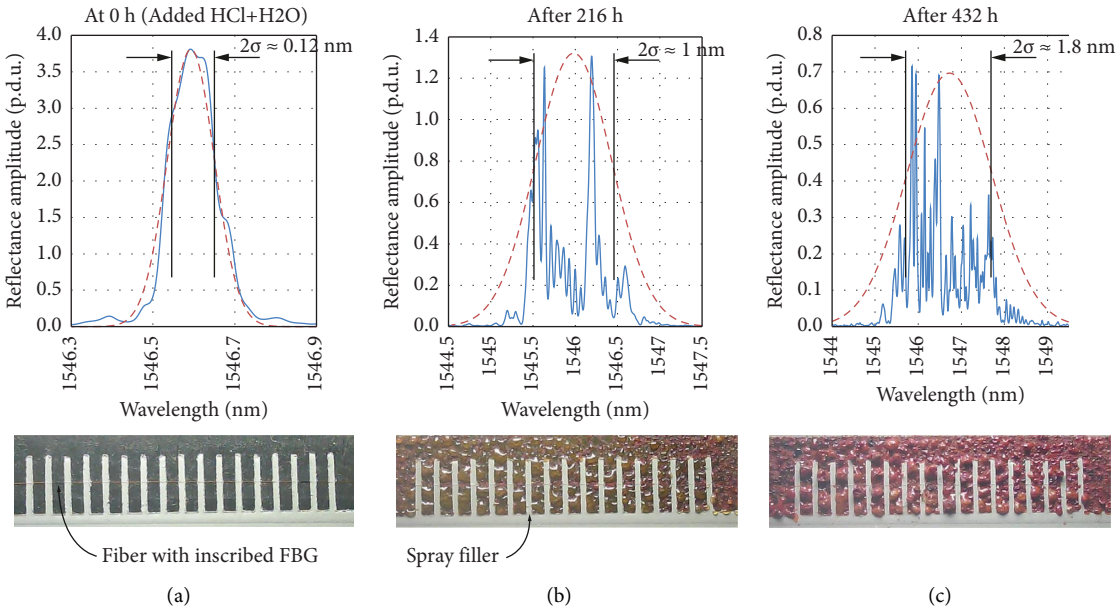

FIGURE 9: Recorded spectrum from the sensor and recorded sample image at (a) The beginning of the test, (b) after 216 hours, and (c) 432 hours (at the end) of the test.

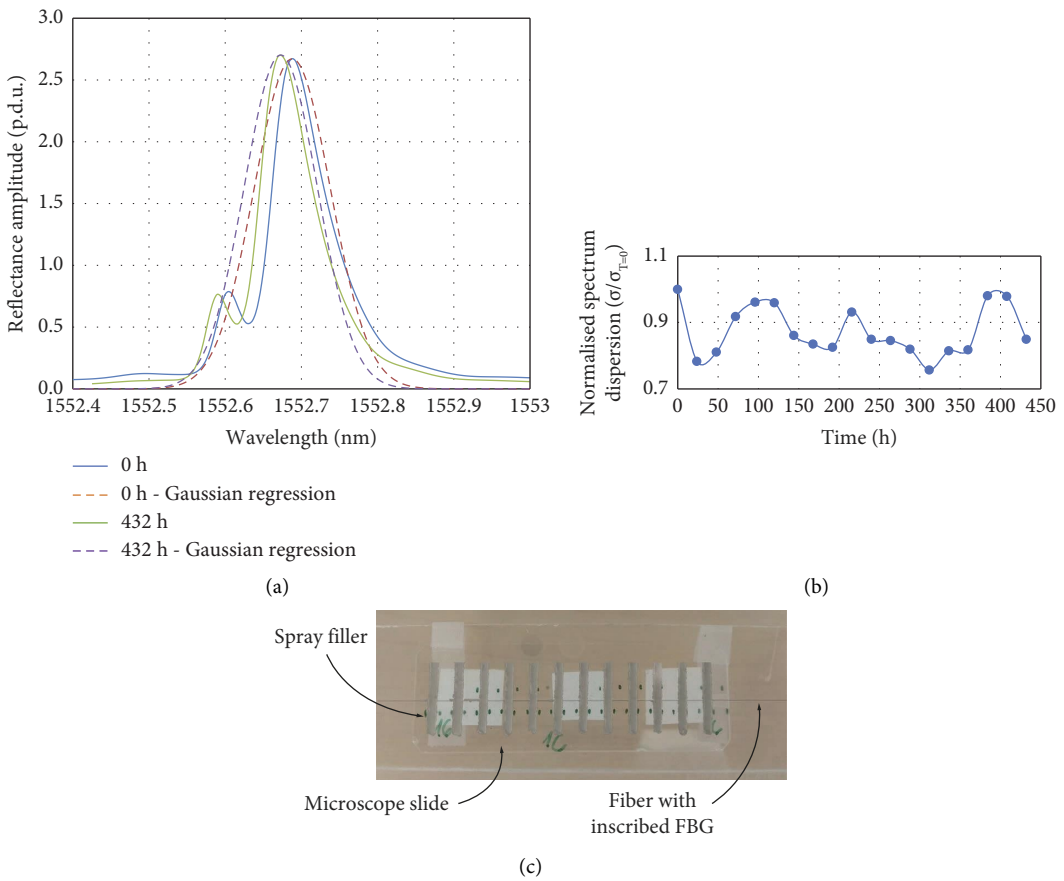

FIGURE 10: (a) Recorded spectrum from the sensor mounted on a microscope glass slide sample at the beginning and at the end of the test with the Gaussian regression for the respective measurement. (b) Calculated normalized spectrum dispersion at different time intervals during the test. (c) Mounted sensor on the glass microscope slide sample by employing spray filler.

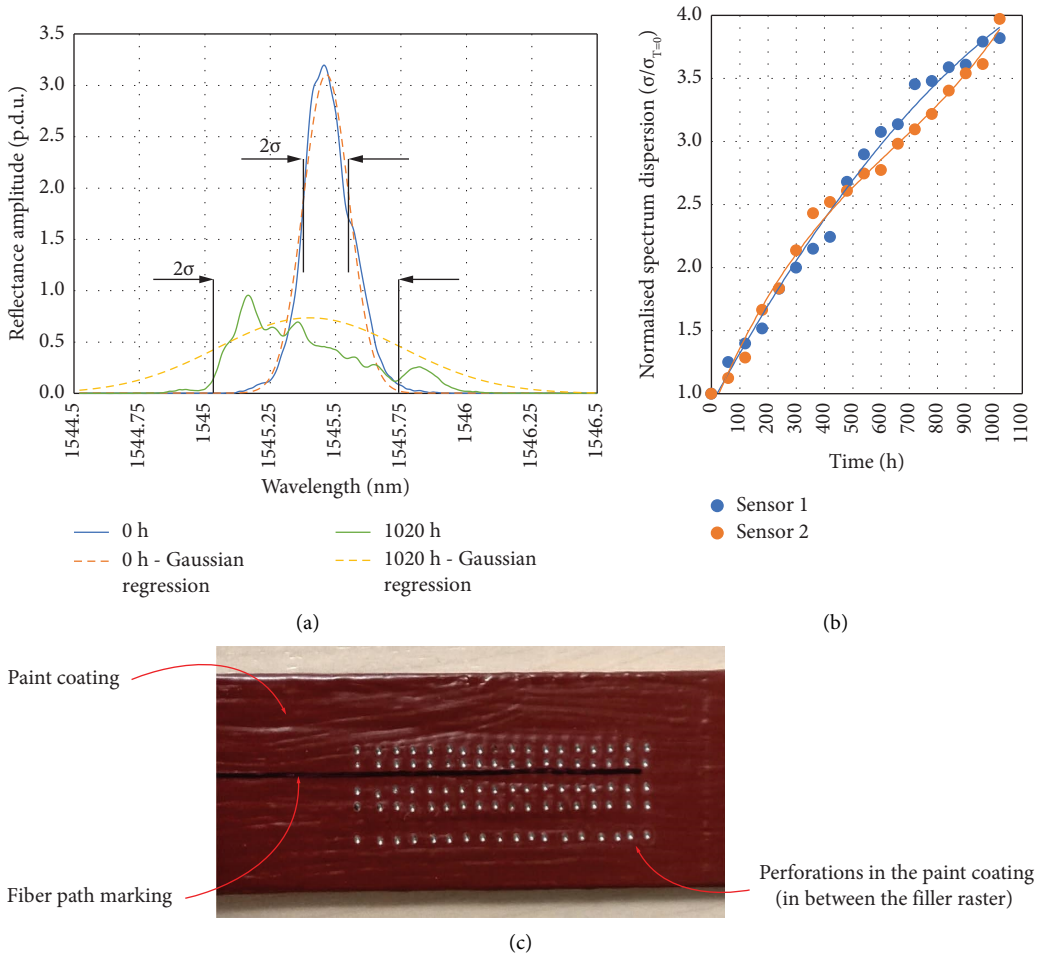

FIGURE 11: (a) Recorded spectrum for the sensor fixed with spray filler on a steel sample coated with a high grade two-component epoxy primer for marine applications at the beginning and at the end of the test with the Gaussian regression for the respective measurement. (b) Calculated normalized spectrum dispersion at different time intervals during the test. (c) Mounted sensor on the steel sample with perforations in the paint coating.

a protective coating over the sensor. Further tests thus employed sensors based on a fiber with a diameter of 80 μm with inscribed 100th-order FBGs, which were further coated with the high-grade two-component epoxy primer for marine applications (Universal yacht primer acquired from Sea Line). Before coating the sample with the sensor by epoxy primer, the sensor was mounted with the adhesive stencil and filler by the method described in the text above. To accelerate the corrosion process, the test sample was punctured through the coating at several locations close to the sensor (Figure 11(c)). The test sample was submerged into the saltwater bath for 40 days. The test results indicated spectrum broadening in the range between 0.5 and 0.7 nm (Figure 11(a)), corresponding to a normalized spectral dispersion increase σ/σ_0 of about 3.5–4 (Figure 11(b)). Although the magnitude of the spectrum degradation was about 3 times lower when compared with the tests conducted on samples without a protective coat, it was feasible to detect corrosion of the steel sample protected by the marine epoxy primer confidently.

Finally, the proposed sensing principle was tested without using the periodically applied spray filler. In this study, the sensor was pretensioned and fixed on the steel sample only with the protective paint coating, as described in the text above. The initial test showed a low, very limited response when using the 80 μm outer diameter fiber; thus, the fiber diameter was reduced further in this experiment to the outer diameter of 50 μm. The sample was coated with 3 thin layers of transparent primer (Figure 12(c)), which also allowed for visual observation of the onset of the corrosion process. The width of the FBG spectrum increased from the initial 0.12 nm to 0.165 nm during mounting/coating, which was a consequence of the high sensitivity of the 50 μm fiber to any perturbations. The later spectrum width was, therefore, set as the starting value for the corrosion test. After exposing the sample for 13 days to the corrosive atmosphere, prepared with added hydrochloric acid (HCl) and water vapors, the sensor's spectrum broadened by 0.142 nm to a cumulative 0.307 nm (Figure 12(a)), thus yielding a normalized spectral dispersion σ/σ_0 increase from 1 to up to 1.85 (Figure 12(b)).

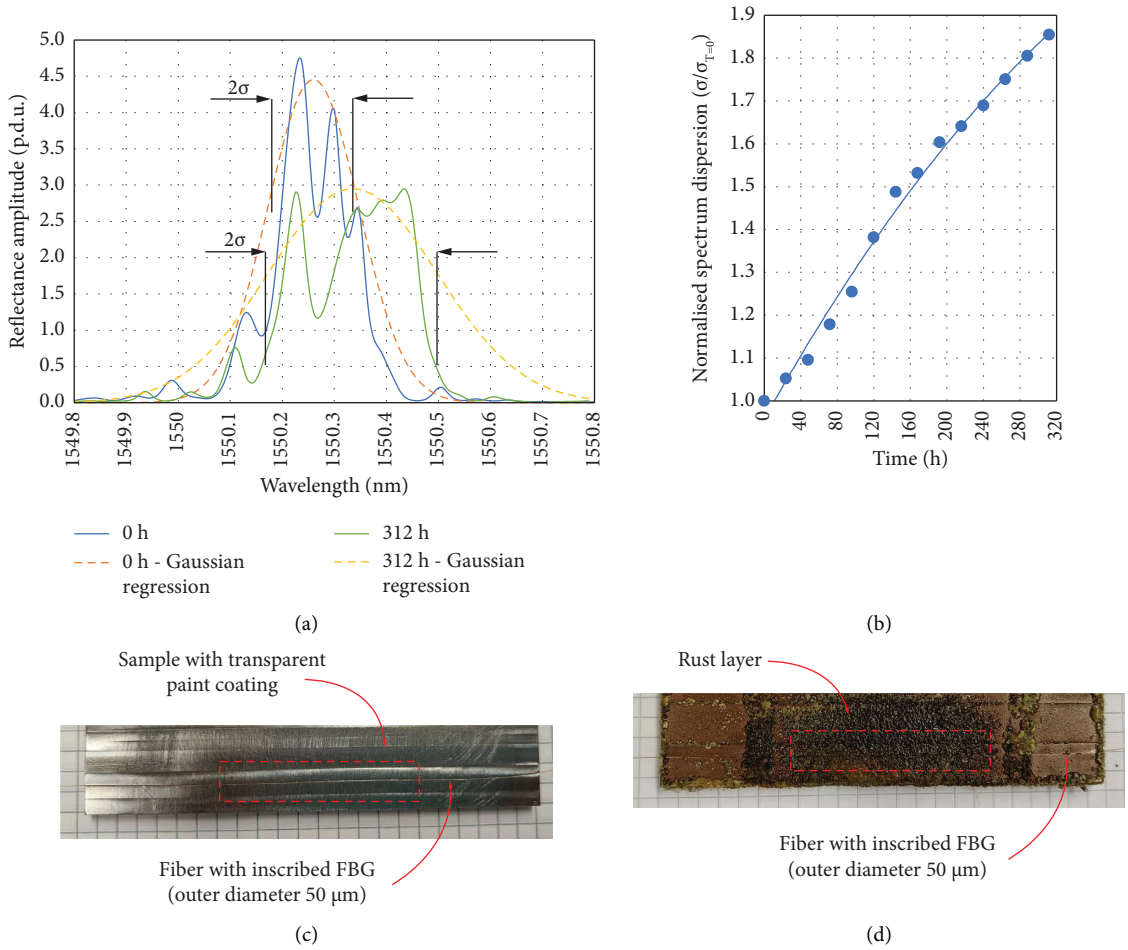

FIGURE 12: (a) Recorded spectrum from the sensor at the beginning and at the end of the test with the Gaussian regression. (b) Calculated normalized spectrum dispersion at different time intervals during the test. (c) Mounted sensor on the steel sample with only a protective primer. (d) Steel sample after the 312-hour test.

5. Conclusion

This paper presented a new method for corrosion detection employing high-order fiber Bragg gratings. When a proper attachment of the high-order FBG to the monitored metal surface is used, random, corrosion-induced surface volumetric expansions of the monitored surface modulate distances between otherwise uniformly spaced FBG's dielectric mirrors. Modulation of these distances between the FBG's mirrors resulted in the FBG's spectral peak widening and spectral peak amplitude reduction, which can be used further to assess the state of the monitored surface.

While investigating different approaches to attach fibers to the monitored metal surfaces, the initial investigation showed no useful responses from sensors built with fibers using a standard outer diameter (125 μm) and 1st-order FBGs. To achieve the desired sensitivity, a reduction of the sensing fiber's outer diameter was necessary. Fibers with outer diameters of 80 μm and 50 μm yielded sensors with a robust response to the formation of an uneven surface beneath the fibers.

The exploration of various mounting techniques also indicated the strong impact of the fiber attachment method on the sensor's response. The application of periodic attachment of the sensing fiber to the surface by periodic application of a relatively hard (high Young's modulus) spray filler yielded highly responsive sensors. For example, when employing fibers with an outer diameter of 80 μm with inscribed 100th-order FBGs, the sensor's initial spectral characteristics broadened by a factor of up to 19 times in comparison with the original spectrum width when no protective coat was applied. This relatively high sensitivity sensor configuration also encouraged tests when the entire sensor was coated by a corrosion-protective layer. Even after applying an epoxy marine-grade protective coat over the sensor, the sensor's spectrum broadened by a factor of about 4 upon provoking corrosion effects beneath the sensor, which is well within the range of reliable detection.

Finally, a direct mounting was also investigated, using only the corrosion-protective coating as the means of fiber attachment to the monitored surface. This approach required further fiber outer diameter reduction. Useful sensing results were obtained when we reduced the sensing fiber's outer diameter to 50 μm while using a 100th-order FBG. In this case, the sensor's spectrum broadened by a factor of about 2 after provoking the corrosion process beneath the

fiber. It should be stressed, however, that a 50 μm sensing fiber with inscribed FBG becomes sensitive to other perturbations, such as, for example, shrinkage of the coating during the curing process; thus, periodic mounting with a hard spray filler might be a more practical approach. This investigation thus presented a strong correlation between the level of spectrum degradation and the degree of corrosion. Tests exhibited repeatable calculated spectrum dispersion when employing FBG sensors with fiber outer diameters of 125 μm, 80 μm, and 50 μm, with the appropriate attachment method. Corrosion detection with the proposed sensor (and signal processing method), which utilizes spectral broadening, is independent of temperature and strain (temperature could be independently read out by observing absolute spectral shift).

In summary, proper attachment of the high-order FBGs inscribed in reduced diameter fibers onto the metal surfaces can yield simple, easy to mount and sensitive corrosion sensors. The proposed sensors can also be mounted beneath the corrosive protective layers and can provide the possibility for minimally obtrusive mounting. For example, the epoxy primer thickness typically exceeds the sensing fiber's diameter, and the mounted sensor integrates well with the protective primer. The demonstrated sensors provided sensitivity which allows for the relatively early corrosion detection. The fabrication method, operation principle, and interrogation approach also allow for this type of sensor to be applied in quasidistributed corrosion detection configurations.

Data Availability

The data used to support the findings of this study are made available from the corresponding author upon reasonable request.

Conflicts of Interest

The authors declare that they have no conflicts of interest.

Acknowledgments

The authors are grateful for the financial support from the Office of Naval Research under Grant no. 12827129 and from the Slovenian Public Research Agency under Grant nos. P2-0028 and P2-0368.

References

[1] M. A. J. Mazumder, "Global impact of corrosion: occurrence, cost and mitigation," *Global Journal of Environmental Sciences*, vol. 5, p. 5, 2020.

[2] R. F. Wright, P. Lu, J. Devkota, F. Lu, M. Ziomek-Moroz, and P. R. Ohodnicki, "Corrosion sensors for structural health monitoring of oil and natural gas infrastructure: a review," *Sensors*, vol. 19, no. 18, p. 3964, 2019.

[3] K. T. Chiang and L. Yang, "High-temperature electrochemical sensor for online corrosion monitoring," *Corrosion-Us*, vol. 66, no. 9, pp. 095002–095008, 2010.

[4] R. B. Figueira, "Electrochemical sensors for monitoring the corrosion conditions of reinforced concrete structures: a review," *Applied Sciences*, vol. 7, no. 11, p. 1157, 2017.

[5] G. Zichao, D. Min, and C. Zhenbang, "Study pitting corrosion of P110 steel by electrochemical frequency modulation technique and coupled multielectrode array sensor," *Corrosion-Us*, vol. 73, no. 8, pp. 998–1006, 2017.

[6] H. Y. Sun, L. J. Sun, Z. W. Liu, and S. L. Zhu, "A smart marine corrosion sensor used in marine survey," *Applied Mechanics and Materials*, vol. 303–306, pp. 128–131, 2013.

[7] J. R. Zhang, C. Liu, M. Sun, and Z. J. Li, "An innovative corrosion evaluation technique for reinforced concrete structures using magnetic sensors," *Construction and Building Materials*, vol. 135, pp. 68–75, 2017.

[8] K. Perveen, G. E. Bridges, S. Bhadra, and D. J. Thomson, "Corrosion potential sensor for remote monitoring of Civil structure based on printed circuit board sensor," *IEEE Transactions on Instrumentation and Measurement*, vol. 63, no. 10, pp. 2422–2431, 2014.

[9] L. Yang, K. T. Chiang, P. K. Shukla, and N. Shiratori, "Internal current effects on localized corrosion rate measurements using coupled multielectrode array sensors," *Corrosion-Us*, vol. 66, no. 11, pp. 115005–115012, 2010.

[10] L. Yang, N. Sridhar, O. Pensado, and D. S. Dunn, "An in-situ galvanically coupled multielectrode array sensor for localized corrosion," *Corrosion-Us*, vol. 58, no. 12, pp. 1004–1014, 2002.

[11] Z. B. Pei, D. W. Zhang, Y. J. Zhi et al., "Towards understanding and prediction of atmospheric corrosion of an Fe/Cu corrosion sensor via machine learning," *Corrosion Science*, vol. 170, Article ID 108697, 2020.

[12] T. Chowdhury, N. D'Souza, Y. H. Ho, N. Dahotre, and I. Mahbub, "Embedded corrosion sensing with ZnO-pvdf sensor textiles," *Sensors*, vol. 20, no. 11, p. 3053, 2020.

[13] F. J. Tang, G. S. Zhou, H. N. Li, and E. Verstrynge, "A review on fiber optic sensors for rebar corrosion monitoring in RC structures," *Construction and Building Materials*, vol. 313, Article ID 125578, 2021.

[14] P. G. Venancio, R. A. Cottis, R. Narayanaswamy, and J. C. S. Fernandes, "Optical sensors for corrosion detection in airframes," *Sensors and Actuators B: Chemical*, vol. 182, pp. 774–781, 2013.

[15] D. Luo, J. N. Li, and Y. Y. Li, "A review of fiber-optic corrosion sensor in Civil engineering," *AIP Conference Proceedings*, vol. 1967, 2018.

[16] L. Li, M. Chakik, and R. Prakash, "A review of corrosion in aircraft structures and graphene-based sensors for advanced corrosion monitoring," *Sensors*, vol. 21, no. 9, p. 2908, 2021.

[17] K. Al Handawi, N. Vahdati, P. Rostron, L. Lawand, and O. Shiryayev, "Strain based FBG sensor for real-time corrosion rate monitoring in pre-stressed structures," *Sensors and Actuators B: Chemical*, vol. 236, pp. 276–285, 2016.

[18] F. D. Deng, Y. Huang, and F. Azarmi, "Corrosion detection for steel with soft coating using in-line fiber Bragg grating sensor," *Sensors and Smart Structures Technologies for Civil Mechanical, and Aerospace Systems*, vol. 10168, 2017.

[19] J. A. Greene, M. E. Jones, P. G. Duncan et al., "Grating-based optical fiber corrosion sensors," *P Soc Photo-Opt Ins*, vol. 3042, pp. 260–266, 1997.

[20] J. Greene, M. Jones, T. Bailey, and I. Perez, "Optical fiber corrosion sensors for aging aircraft," *SPIE Proceedings Series*, vol. 3399, pp. 28–33, 1998.

[21] X. Liang, Y. Huang, S. A. Galedari, and F. Azarmi, "Pipeline corrosion assessment using embedded fiber Bragg grating

sensors," *Sensors and Smart Structures Technologies for Civil Mechanical, and Aerospace Systems*, vol. 9435, 2015.

[22] J. Ma, B. Lu, D. Sun, Z. Wang, and X. F. Zhao, "Experimental study on a novel corrosion sensor for steel strand using FBG," *Sensors and Smart Structures Technologies for Civil, Mechanical, and Aerospace Systems*, vol. 11591, 2021.

[23] O. Shiryayev, M. Cullin, and R. Srinivasan, "On the development of an improved magnetic-based corrosion sensor," *Sensors and Smart Structures Technologies for Civil, Mechanical, and Aerospace Systems*, vol. 11591, 2021.

[24] L. H. Cai, W. Li, and H. F. Fang, "Characterization of Fe-C alloy film optical fiber corrosion sensors by fractal," *Advanced Materials Research*, vol. 239–242, pp. 976–980, 2011.

[25] C. R. Guo, L. Fan, C. L. Wu, G. D. Chen, and W. Li, "Ultrasensitive LPFG corrosion sensor with Fe-C coating electroplated on a Gr/AgNW film," *Sensors and Actuators B: Chemical*, vol. 283, pp. 334–342, 2019.

[26] S. Abderrahmane, A. Himour, R. Kherrat, E. Chailleux, N. Jaffrezic-Renault, and G. Stremsdoerfer, "An optical fibre corrosion sensor with an electroless deposit of Ni-P," *Sensors and Actuators B: Chemical*, vol. 75, no. 1-2, pp. 1–4, 2001.

[27] W. B. Hu, H. L. Cai, M. H. Yang, X. L. Tong, C. M. Zhou, and W. Chen, "Fe-C-coated fibre Bragg grating sensor for steel corrosion monitoring," *Corrosion Science*, vol. 53, no. 5, pp. 1933–1938, 2011.

[28] X. Zheng, W. B. Hu, N. Zhang, and M. Gao, "Optical corrosion sensor based on fiber Bragg grating electroplated with Fe-C film," *Optical Engineering*, vol. 53, no. 7, Article ID 077104, 2014.

[29] X. M. Li, W. M. Chen, Z. Q. Huang, S. L. Huang, and K. D. Bennett, "Fiber optic corrosion sensor fabricated by electrochemical method," *Smart Structures and Materials*, vol. 3330, pp. 126–133, 1998.

[30] P. Y. Aisyah, A. M. Hatta, and D. Y. Pratama, "Design of SMS (single mode-multi mode coreless-single mode) optical fiber as corrosion sensor," in *Proceedings of the 2nd International Seminar on Photonics, Optics, and its Applications (Isphoa 2016)*, p. 10150, Bali, Indonesia, August 2016.

[31] P. Giaccari, G. R. Dunkel, L. Humbert, J. Botsis, H. G. Limberger, and R. P. Salathe, "On a direct determination of non-uniform internal strain fields using fibre Bragg gratings," *Smart Materials and Structures*, vol. 14, no. 1, pp. 127–136, 2005.

[32] H. Huang and S. Yuan, "Study on the spectral response of fiber Bragg grating sensor under non-uniform strain distribution in structural health monitoring," *Optoelectronics Letters*, vol. 7, no. 2, pp. 109–112, 2011.

[33] P. Kisala, "Measurement of the maximum value of non-uniform strain using a temperature-insensitive fibre Bragg grating method," *Opto-Electronics Review*, vol. 21, no. 3, pp. 293–302, 2013.

[34] H. Y. Ling, K. T. Lau, L. Cheng, and K. W. Chow, "Embedded fibre Bragg grating sensors for non-uniform strain sensing in composite structures," *Measurement Science and Technology*, vol. 16, no. 12, pp. 2415–2424, 2005.

[35] A. Rajabzadeh, R. Heusdens, R. C. Hendriks, and R. M. Groves, "Calculation of the mean strain of smooth non-uniform strain fields using conventional FBG sensors," *Journal of Lightwave Technology*, vol. 36, no. 17, pp. 3716–3725, 2018.

[36] S. Yashiro, N. Takeda, T. Okabe, and H. Sekine, "A new approach to predicting multiple damage states in composite laminates with embedded FBG sensors," *Composites Science and Technology*, vol. 65, no. 3-4, pp. 659–667, 2005.

[37] F. D. Zhu, D. S. Zhang, P. Fan, L. T. Li, and Y. X. Guo, "Non-uniform strain measurement along a fiber Bragg grating using optical frequency domain reflectometry," *Chinese Optics Letters*, vol. 11, no. 10, Article ID 100603, 2013.

[38] D. H. Kang, S. O. Park, C. S. Hong, and C. G. Kim, "The signal characteristics of reflected spectra of fiber Bragg grating sensors with strain gradients and grating lengths," *NDT and E International*, vol. 38, no. 8, pp. 712–718, 2005.

[39] Q. P. Liu, X. G. Qiao, Z. A. Jia, and H. W. Fu, "Spectra power and bandwidth of fiber Bragg grating under influence of gradient strain," *Photonic Sens*, vol. 6, no. 4, pp. 333–338, 2016.

[40] M. Kharshiduzzaman, A. Gianneo, and A. Bernasconi, "Experimental analysis of the response of fiber Bragg grating sensors under non-uniform strain field in a twill woven composite," *Journal of Composite Materials*, vol. 53, no. 7, pp. 893–908, 2019.

[41] P. C. Hill and B. J. Eggleton, "Strain gradient chirp of fibre Bragg gratings," *Electronics Letters*, vol. 30, no. 14, pp. 1172–1174, 1994.

[42] C. W. Zhang, Z. S. Alam, L. Sun, Z. X. Su, and B. Samali, "Fibre Bragg grating sensor-based damage response monitoring of an asymmetric reinforced concrete shear wall structure subjected to progressive seismic loads," *Structural Control and Health Monitoring*, vol. 26, no. 3, Article ID e2307, 2019.

[43] V. Matveenko, G. Serovaev, N. Kosheleva, and A. Fedorov, "Numerical and experimental analysis of the reliability of strain measured by surface-mounted fiber-optic sensors based on Bragg gratings," *Structural Control and Health Monitoring*, vol. 29, no. 12, 2022.

[44] M. Bravo, C. McCague, M. Fabian et al., "Reinforced concrete structural corrosion monitoring using Hi-Bi photonic crystal fibres in a fiber loop structure," in *Proceedings of the 23rd International Conference on Optical Fibre Sensors*, p. 9157, Santander, Spain, June 2014.

[45] C. McCague, M. Fabian, M. Karimi, T. Sun, and K. T. V. Grattan, "Novel distributed sensor design for corrosion monitoring using photonic crystal fibers," in *Proceedings of the 2013 IEEE 6th International Conference on Advanced Infocomm Technology (ICAIT)*, pp. 17-18, Hsinchu, Taiwan, July 2013.

[46] D. Turkmen, A. Krug, and B. Mizaikoff, "Monitoring corrosion processes via visible fiber-optic evanescent wave sensor," *Chemosensors*, vol. 8, no. 3, p. 76, 2020.

[47] D. Luo, Y. Y. Li, T. Lu, K. S. Lim, and H. Ahmad, "Tapered polymer optical fiber sensors for monitoring the steel bar corrosion," *IEEE Transactions on Instrumentation and Measurement*, vol. 70, pp. 1–9, 2021.

[48] M. Maalej, S. F. U. Ahmed, K. S. C. Kuang, and P. Paramasivam, "Fiber optic sensing for monitoring corrosion-induced damage," *Structural Health Monitoring*, vol. 3, no. 2, pp. 165–176, 2004.

[49] X. Tan, L. Fan, Y. Huang, and Y. Bao, "Detection, visualization, quantification, and warning of pipe corrosion using distributed fiber optic sensors," *Automation in Construction*, vol. 132, Article ID 103953, 2021.

[50] J. F. Martins-Filho, E. Fontana, J. Guimaraes, and I. J. S. Coelho, "Multipoint fiber-optic-based corrosion sensor," *Proceedings of SPIE*, vol. 7004, 2008.

[51] L. Fan, Y. Bao, and G. Chen, "Feasibility of distributed fiber optic sensor for corrosion monitoring of steel bars in reinforced concrete," *Sensors*, vol. 18, no. 11, p. 3722, 2018.

[52] M. Njegovec, V. Budinski, B. Macuh, and D. Donlagic, "Microbend point and distributed fiber optic corrosion sensing," *IEEE Transactions on Instrumentation and Measurement*, vol. 71, pp. 1–12, 2022.

[53] A. Fedorov, V. Lazarev, I. Makhrov et al., "Structural monitoring system with fiber Bragg grating sensors: implementation and software solution," *Journal of Physics: Conference Series*, vol. 594, Article ID 012049, 2015.

[54] P. V. R. Shekar, D. M. Latha, K. Kumari, and V. G. Pisipati, "Optimal parameters for fiber Bragg gratings for sensing applications: a spectral study," *SN Applied Sciences*, vol. 3, no. 6, p. 666, 2021.

[55] H. Sze Phing, J. Ali, R. Abdul Rahman, and B. Ahmed Tahir, "Fiber Bragg grating modeling, simulation and characteristics with different grating lengths," *Malaysian Journal of Fundamental and Applied Sciences*, vol. 3, no. 2, 2007.

[56] Y. Dong and D. M. Frangopol, "Risk-informed life-cycle optimum inspection and maintenance of ship structures considering corrosion and fatigue," *Ocean Engineering*, vol. 101, pp. 161–171, 2015.

[57] A. Zayed, Y. Garbatov, and C. G. Soares, "Reliability of ship hulls subjected to corrosion and maintenance," *Structural Safety*, vol. 43, pp. 1–11, 2013.

[58] D. D. Zhang, J. Wu, and J. Q. Gao, "Investigation and detection on corrosion of concrete structure in marine environment," *Second International Conference on Smart Materials and Nanotechnology in Engineering*, vol. 7493, 2009.

[59] C. Iandiorio and P. Salvini, "An analytical solution for large displacements of end-loaded beams," in *Proceedings of the 1st International Conference on Numerical Modelling in Engineering*, pp. 320–338, Springer, Singapore, 2019.

[60] W. Jrad, F. Mohri, G. Robin, E. M. Daya, and J. Al-Hajjar, "Analytical and finite element solutions of free and forced vibration of unrestrained and braced thin-walled beams," *Journal of Vibration and Control*, vol. 26, no. 5-6, pp. 255–276, 2020.

[61] C. A. Moreira, G. B. Barbat, M. Cervera, and M. Chiumenti, "Accurate thermal-induced structural failure analysis under incompressible conditions," *Engineering Structures*, vol. 261, Article ID 114213, 2022.

[62] L. Skec, G. Alfano, and G. Jelenic, "Complete analytical solutions for double cantilever beam specimens with bi-linear quasi-brittle and brittle interfaces," *International Journal of Fracture*, vol. 215, no. 1-2, pp. 1–37, 2019.

[63] M. Vaz, P. A. Munoz-Rojas, and G. Filippini, "On the accuracy of nodal stress computation in plane elasticity using finite volumes and finite elements," *Computers and Structures*, vol. 87, no. 17, pp. 1044–1057, 2009.

[64] A. Zorić, M. Trajkovic-Milenkovic, D. Zlatkov, and T. Vacev, "Semi-Analytical solution for elastoplastic deflection of non-prismatic cantilever beams with circular cross-section," *Applied Sciences*, vol. 12, no. 11, p. 5439, 2022.

[65] M. Attarchi, A. Brenna, and M. Ormellese, "FEM simulation of corrosion under macro-cell mechanism," *Corrosion Science*, vol. 179, Article ID 109116, 2021.

[66] Y. L. Chen, H. L. Huang, Y. Zhang, G. X. Bian, C. G. Wang, and A. D. Wang, "A finite element model (FEM) for predicting the corrosion of multi-material coupling system on aircrafts," *Materials and Corrosion*, vol. 69, no. 11, pp. 1649–1657, 2018.

[67] M. German and J. Pamin, "FEM simulations of cracking in RC beams due to corrosion progress," *Archives of Civil and Mechanical Engineering*, vol. 15, no. 4, pp. 1160–1172, 2015.

[68] C. Liu and R. G. Kelly, "A review of the application of finite element method (FEM) to localized corrosion modeling," *Corrosion-Us*, vol. 75, no. 11, pp. 1285–1299, 2019.

[69] L. T. Yin, Y. Jin, C. Leygraf, and J. S. Pan, "A FEM model for investigation of micro-galvanic corrosion of Al alloys and effects of deposition of corrosion products," *Electrochimica Acta*, vol. 192, pp. 310–318, 2016.

[70] H. Fang and M. Duan, "Chapter 6-submarine pipelines and pipeline cable engineering," in *Offshore Operation Facilities*, pp. 1–181, Gulf Professional Publishing, Boston, MA, USA, 2014.